Research Article

Nano Research
2022, 15(5): 4014–4022

ISSN 1998-0124 CN 11-5974/O4
https://doi.org/10.1007/s12274-022-4177-x

Tuning the reaction path of CO_2 electroreduction reaction on indium single-atom catalyst: Insights into the active sites

Jiawei Zhang[1,§], Gangming Zeng[1,§], Lanlan Chen[2,§], Wenchuan Lai[1], Yuliang Yuan[1], Yangfan Lu[3], Chao Ma[1], Wenhua Zhang[2] (✉), and Hongwen Huang[1] (✉)

[1] *College of Materials Science and Engineering, Advanced Catalytic Engineer Research Center of the Ministry of Education, Hunan University, Changsha 410082, China*
[2] *Hefei National Laboratory for Physical Sciences at the Microscale, Key Laboratory of Strongly-Coupled Quantum Matter Physics of Chinese Academy of Sciences, Department of Chemical Physics, University of Science and Technology of China, Hefei 230026, China*
[3] *State Key Lab of Silicon Materials, School of Materials Science and Engineering, Zhejiang University, Hangzhou 310027, China*
[§] *Jiawei Zhang, Gangming Zeng, and Lanlan Chen contributed equally to this work.*

Received: 2 January 2022 / **Revised:** 13 January 2022 / **Accepted:** 17 January 2022

ABSTRACT

Modulating the local coordination structure of metal single-atom catalysts (SACs) is extensively employed to tune the catalytic activity, but rarely involved in regulating the reaction pathway which fundamentally determines the product selectivity. Herein, we report that the product selectivity of electrochemical CO_2 reduction (CO_2RR) on the single-atom indium-N_xC_{4-x} ($1 \le x \le 4$) catalysts could be tuned from formate to CO by varying the carbon and nitrogen occupations in the first coordination sphere. Surprisingly, the optimal In SAC showed great promise for CO production with the maximum Faradic efficiency of 97%, greatly different from the reported In-based catalysts where the formate is the dominant product. Combined experimental verifications and theoretical simulations reveal that the selectivity switch from formate to CO on In SACs originates from active sites shift from indium center to the indium-adjacent carbon atom, where the indium site favors formate formation and the indium-adjacent carbon site prefers the CO pathway. The present work suggests the active sites in metal SACs may shift from the widely accepted metal center to surrounding carbon atoms, thereby offering a new implication to revisit the active sites for metal SACs.

KEYWORDS

CO_2 reduction, single atom catalysts, coordination structure, product selectivity, active sites shift

1 Introduction

Accumulation of anthropogenic CO_2 has aroused serious climate issues, and electrochemical CO_2 reduction (CO_2RR) into chemical feedstocks powered by renewable sources has emerged as a "two birds in one stone" strategy to establish a carbon-neutral cycle and store intermittent energy in a sustainable manner [1–5]. Nevertheless, technological viability of the CO_2RR process relies on affordable and efficient catalysts due to the high thermodynamic stability of CO_2 molecules, the complex proton-coupled multi-electron pathways, as well as the more kinetically favorable hydrogen evolution reaction (HER) in aqueous medium [6–9]. Since Hori's landmark discovery on CO_2RR in the 1980s [10, 11], a plethora of catalysts have demonstrated their remarkable CO_2RR activity [12–15], of them, single atom catalysts (SACs) featuring ~ 100% atom utilization efficiency and well-defined structure have received considerable attention owing to their unprecedented activity toward CO_2RR [16–19].

Enabled by the coordination unsaturated environment of atomically dispersed metal center, the SACs usually exhibit distinct catalytic properties compared with corresponding bulk materials owing to their unique affinity toward reaction intermediates [20–26]. Presently, engineering the coordination structure of active sites represents an effective strategy to optimize catalytic activity of SACs [27–34]. For instance, considerable enhancement on CO_2RR activity was observed upon decreasing the Co–N coordination number of Co SACs from 4 to 2, where the enhanced activity was ascribed to the accelerated CO_2 activation process upon lowering the coordination number [33]. In addition to the activity enhancement, a few recent studies also suggested the potential impacts of coordination structure on the reaction pathway for CO_2RR, which fundamentally determines the product selectivity. In a typical example, two Sb SACs derived from different precursors showed distinct selectivity toward CO_2RR, the Sb NC catalyst exhibited excellent selectivity for CO production with Faraday efficiency (FE_{CO}) above 82.0% [35], while ~ 94% FE_{HCOOH} was obtained over the Sb-N_4 catalyst [36]. Despite these observations, the chemical insight into the distinct product selectivity on these SACs for CO_2RR has never been provided so far.

Very recently, Qiao et al. demonstrated the tailoring of the oxygen reduction reaction (ORR) reaction pathway on Co SACs from a four-electron to a two-electron pathway by modifying the coordination spheres, confirming the feasibility in manipulating the reaction pathway via tuning the local coordination environment of SACs [37]. Inspired by their work, we herein, for

Address correspondence to Wenhua Zhang, whhzhang@ustc.edu.cn; Hongwen Huang, huanghw@hnu.edu.cn

the first time, report that the product selectivity of CO_2RR on the single-atom indium-N_xC_{4-x} ($1 \le x \le 4$) catalysts could be tuned from formate to CO by varying the carbon and nitrogen occupations in the first coordination sphere. As demonstrated by a combination of experimental evidences and density functional theory (DFT) calculations, formation of formate and CO originates from distinct active sites in In SACs: The indium center favors formate formation while indium-adjacent carbon atoms gradually turned into active sites for CO generation with the increased carbon occupation in the first coordination sphere of In SACs.

2 Experimental

2.1 Chemicals and materials

Indium nitrate hydrate ($In(NO_3)_3{\cdot}4H_2O$), potassium bicarbonate ($KHCO_3$), terephthalic acid ($C_8H_6O_4$), dicyandiamide ($C_2H_4N_4$), N, N-dimethylformamide (DMF), and ethanol (C_2H_5OH) were all purchased from Sinopharm Chemical Reagent Co., Ltd. (Shanghai, China). All the chemicals were used without further purification. Ultrapure Millipore water (18.2 MΩ) was used in all our experiments.

2.2 Synthesis of In metal organic framework (MOF) (MIL-68)

In a typical experiment, 0.5 mmol 1,4-benzenedicarboxylic acid (H_2BDC) was dissolved in 10 mL of DMF, followed by addition of 0.25 mmol $In(NO_3)_3{\cdot}4H_2O$. The resulting reaction mixture was stirred at room temperature for 20 min and then placed in a preheated oil bath (120 °C) for 60 min. The as-obtained white precipitates were centrifuged, washed with distilled water and absolute ethanol for three times respectively, and dried in vacuum at 60 °C for 5 h.

2.3 Synthesis of In SACs

The as-prepared MIL-68(In) precursor (100 mg) was mixed with dicyandiamide (1.0 g) by grinding, the mixture was heated under 550 °C for 3 h before being heated at desired temperature (heating rate 3 °C·min^{-1}) for 1 h under argon atmosphere at a flow rate of 50 sccm. The residual after pyrolysis was leached with 1 M HCl at 80 °C for 12 h to remove possible cluster residues. For In SACs fabricated at different temperature (800 and 1,000 °C), the catalysts were denoted as In SACs-800 and In SACs-1000 respectively.

2.4 Synthesis of In_2O_3 nanoparticles (NPs)

318.8 mg $In(NO_3)_3{\cdot}4H_2O$ and 500 mg polyvinylpyrrolidone were dissolved in 5 mL deionized (DI) water, the mixture was stirred at room temperature for 0.5 h followed by addition of 10 mL NaOH solution (0.3 M). The reaction mixture was stirred at room temperature for another 0.5 h, the white precipitates were centrifuged, washed with distilled water and absolute ethanol for three times respectively. The white precipitates were dried in vacuum at 60 °C for 5 h and then annealed at 550 °C for 1 h under air to yield In_2O_3 NPs (light yellow powder).

2.5 Electrochemical measurements

Prior to the electrochemical measurements, the working electrode was prepared. Typically, 5.0 mg of In SACs and 25 μL of Nafion solution (5 wt.%) were dispersed in 1 mL of ethanol by sonicating for 1 h to form a homogeneous catalyst ink, the reference carbon supported In_2O_3 NPs catalyst ink was prepared by dispersing 4.0 mg of the In_2O_3 NPs and 4.0 mg of carbon (Vulcan XC-72) into 1.0 mL ethanol through sonicating for 1 h followed by addition of 20 μL Nafion solution (5 wt.%). The catalyst ink was then air brushed onto the gas diffusion layer (GDL, YLS-30T) with a loading of 1 mg·cm^{-2}. For a typical H-cell, the Pt wire and Ag/AgCl (3 M KCl) electrode were used as the counter electrode and reference electrode, and a nickel foam was applied as the anode in the case of flow cell. A mass flow controller was used to set the CO_2 flow rate at 50 sccm. All potentials were measured against an Ag/AgCl reference electrode and calibrated with respect to reversible hydrogen electrode (RHE): E (vs. RHE) = E (vs. Ag/AgCl) + 0.21 V + 0.0592 × pH. All the electrocatalytic reactions were conducted at ambient pressure and temperature and the applied potentials were presented without *iR* correction.

The linear sweep voltammetry (LSV) was performed in CO_2-saturated and argon-saturated 0.5 M $KHCO_3$ aqueous solution from 0 to −1.2 V at a scan rate of 10 mV·s^{-1}. Electrochemical active surface area (ECSA) of the catalysts were estimated by the electrochemical capacitance measurements. Those catalysts were tested with scan rates ranging from 2 to 14 mV·s^{-1} with an interval of 2 mV·s^{-1} at the potential window of 0 to 0.1 V. The extraction of the double-layer capacitances of the samples, the electrochemical double-layer capacitance (C_{dl}), was estimated by plotting j_a–j_c at 0.05 V against the scan rate, where the slope was twice that of C_{dl}. The electrochemical impedance spectra of the samples were recorded with alternating current (AC) voltage with 5 mV amplitude within the frequency range from 0.01 to 100,000 Hz. Tafel slopes for CO production were calculated from the corresponding current densities at the potential range from −0.3 to −0.38 V. The electrochemical reduction of CO_2 was carried out in CO_2-saturated 0.5 M $KHCO_3$ electrolyte (pH = 7.2) in the potential range of −0.5 to −0.8 V at room temperature. Controlled potential electrolysis was conducted at each potential for 45 min, the oxygen generated at the anode was vented out of the reservoir. The gas products of CO_2 electrocatalytic reduction were monitored by an online micro gas chromatography (GC) (GC2014, Shimadzu, Japan) equipped with a TCD detector every 6 min, the catholyte after electrolysis was collected and analyzed on a 400 MHz NMR spectrometer to quantify liquid products.

3 Results and discussion

As illustrated in Fig. 1(a), the atomically dispersed In SACs was crafted using MIL-68(In) as the metal precursor and dicyandiamide as the nitrogen source. The reason why MIL-68(In) was chosen as the metal precursor is that the coordinated oxygen atom and the connected carbon atoms around the indium sites can be primarily removed under high temperature, thus providing great possibility in tailoring the coordination structure of the In SACs [34]. Moreover, the spatially separated indium atoms in MIL-68(In) could decrease the migration of the adjacent metal nodes to a large extent upon thermal treatment [38–41]. Adopting $In(NO_3)_3{\cdot}4H_2O$ as the metal precursor resulted in severe aggregation, and dicyandiamide was chosen as the auxiliary precursor to suppress large-scale aggregation since direct pyrolysis of MIL-68(In) lead to the formation of metal (oxide)/carbon composite structure. The MIL-68(In) (Fig. S1 in the Electronic Supplementary Material (ESM)) was firstly synthesized via a solvothermal method (detail process could be found in the ESM). The as crafted MIL-68(In) was then mixed with dicyandiamide and annealed under argon atmosphere for 2 h, during which the precursors were pyrolyzed to form indium-dispersed N-doped carbon framework. Subsequently, acid leaching was carried out to remove any metallic debris, while the nitrogen-coordinated indium atoms were retained in the nitrogen doped carbon framework. Since the elevated temperature would lead to the decay of metal–N bonds, the local coordination environment of

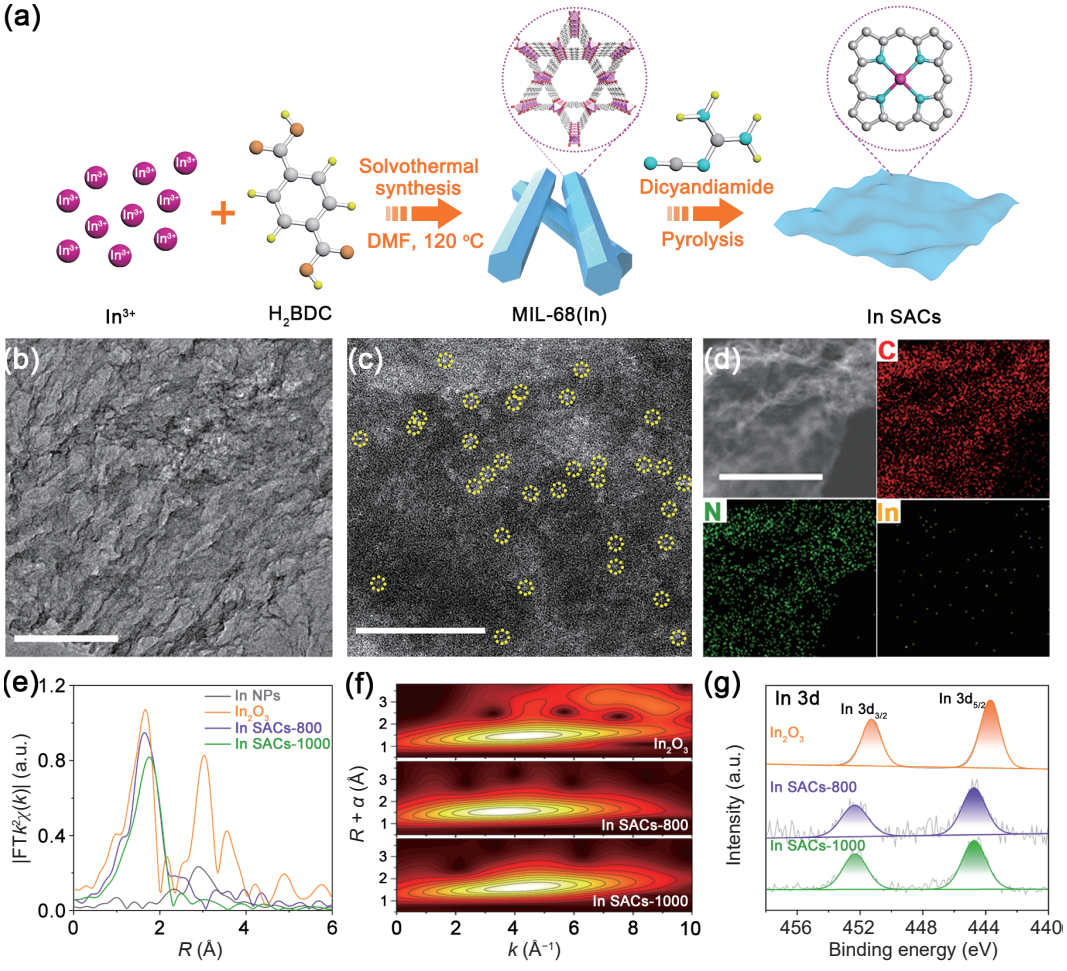

Figure 1 Crafting process and structural characterizations. (a) Schematic illustration for the fabrication of In SACs. (b) Low-magnification TEM image for In SACs-1000. Scale bar is 200 nm. (c) Atomic-resolution HAADF-STEM image for In SACs-1000. Scale bar is 2 nm. (d) EDX elemental mapping images of C, N, and In for In SACs-1000. Scale bar is 50 nm. (e) FT-EXAFS spectra in *R* space of the In SACs catalyst, In foil, and In_2O_3. (f) WT-EXAFS plots of In-SACs and In_2O_3. (g) High-resolution XPS spectra for In 3d of In SACs and In_2O_3.

the indium center was tailored by changing the annealing temperature [33]. As a result, two atomically dispersed In SACs were synthesized and designated as In SACs-*T* (where *T* represents the annealing temperature).

The structural characterizations were then conducted to confirm the formation of atomically dispersed In SACs. The X-ray diffraction (XRD) patterns of the samples showed in Fig. S2 in the ESM only presented a broad peak centered around 24.1°, which can be assigned to the interlayer distance of the carbon matrix [4, 42–44], suggesting the absence of crystalline species of metallic In or In_2O_3 in the products. Transmission electron microscopy (TEM) images of the In SACs catalysts demonstrated their wrinkled sheet-like features (Fig. 1(b), and Figs. S3(a) and S3(b) in the ESM), and no NPs were observed. Atomic dispersion of the indium atoms was directly monitored by the high-angle annular dark-field scanning transmission electron microscopy (HAADF-STEM). The bright dots correspond to indium atoms (highlight by yellow dash circles) homogeneously dispersed throughout the whole catalyst without obvious aggregation (Fig. 1(c) and Fig. S3(c) in the ESM). Moreover, it could be resolved from the HAADF-STEM images that the In SACs-800 possessed higher indium loading than that of the In SACs-1000, which was in line with the inductively coupled plasma atomic emission spectrometry (ICP-AES) results (10.73 wt.% for In SACs-800 and 1.86 wt.% for In SACs-1000). Energy-dispersive X-ray spectroscopy (EDX) of In SACs (Fig. 1(d) and Fig. S3(d) in the ESM) indicated the uniform distribution of C, N, and In over the catalyst, suggesting the successful synthesis of atomically dispersed indium atoms on N-doped carbon.

The local coordination structure and electronic structure of the In SACs were further explored by X-ray absorption spectroscopy (XAS). As indicated in the In K-edge X-ray absorption near edge structure (XANES) spectra (Fig. S4 in the ESM), absorption edge of In SACs-800 is nearly overlapped with In_2O_3, and that of In SACs-1000 is even higher, indicating the positively charged indium centers in the In SACs, which is consistent with data reported in previous work [42, 45, 46]. The Fourier transform (FT) of the In SACs extended X-ray absorption fine structure (EXAFS) (Fig. 1(e)) showed the dominant contribution of a first-shell peak around 1.65 Å (uncorrected phase shift) associated with the coordination of In–X (X represents light elements like C, N, and O), but it is hard to distinguish the exact coordination element due to their similar bond length [47]. Concurrently, no strong contribution was observed around 2.91 and 3.03 Å, which were In–In coordination characteristic for metallic In and In_2O_3, respectively, corroborating the atomic dispersion of indium species in the carbon matrix. Wavelet transform (WT)-EXAFS (with high resolution in both *k* and *R* space) was also performed (Fig. 1(f)), WT signal related to In–X was observed while signals derived from In–In contribution were invisible, further demonstrating the atomic dispersion of indium. Notably, the distinct WT contour maximum for In SACs-800 and In SACs-1000 confirmed that bond length and moiety structure in these two catalysts are different, suggesting the successful tuning of local coordination structure. The fitting results of the In K-edge EXAFS spectrum identified four first-shell light atoms at 2.15 Å in the In

SACs-1000, while one additional axial atom was found in the case of In SACs-800 (Fig. S6 and Table S1 in the ESM). Given that the SACs were crafted under high temperature, the indium center was proposed to coordinate with four in-plane C or N atoms considering that oxygen species are unstable under a carbon thermal condition. Hence, the In-N_xC_{4-x} ($1 \le x \le 4$) structure was established for the In SACs-1000, while the extra axial atom observed in In SACs-800 was attributed to the adsorbed oxygen when exposed to air. Since the adsorbed oxygen could be easily removed under negative bias, the In-N_xC_{4-x} ($1 \le x \le 4$) structure was therefore employed in the following DFT calculation section [47]. X-ray photoelectron spectroscopy (XPS) was also conducted to unveil the chemical states and electronic structures of the In SACs (Figs. S8–S10 in the ESM). The nitrogen content in In SACs determined by XPS was decreased from 20.69% to 4.93% upon elevating the annealing temperature from 800 to 1,000 °C (Table S3 in the ESM). Given the strong coordination strength of nitrogen toward the metal sites, the high nitrogen content would increase nitrogen coordination to the indium center, while carbon occupation in the first coordination sphere of the In-N_xC_{4-x} would be increased in the case of relative low nitrogen content. Moreover, the decreased nitrogen content in In SACs-1000 also rationalized the decreased indium loading upon elevating the annealing temperature in the SACs fabrication process. High-resolution XPS was then employed to investigate the chemical state of In and N in In SACs. As illustrated in the In 3d XPS spectrum (Fig. 1(g)), binding energy in In SACs showed positive shift compared with that of In_2O_3 NPs, which indicates the more electro-deficient nature of the indium center in the In SACs, implying the formation of In–N bond located at ~ 445 eV [42]. The N 1s spectra (Figs. S9(c) and S10(c) in the ESM) were deconvoluted into pyridinic (398.1 eV), pyrrolic (400.9 eV), and graphitic (403.0 eV) in In SACs. Note that the peak at 399.2 eV revealed the presence of porphyrin-like moieties assigned to the metal–nitrogen coordination [42, 48]. Taken together, these characterizations confirmed the successfully fabrication of In SACs with local coordination structure of In-N_xC_{4-x}, where the carbon and nitrogen occupations in the first coordination sphere were regulated by changing the annealing temperature.

The electrocatalytic properties of In SACs for CO_2RR were then evaluated in a customized H-cell using CO_2-saturated 0.5 M $KHCO_3$ solution as electrolyte. As a comparison, the In_2O_3 NPs with an average size of 30 nm were also studied (Fig. S11 in the ESM). As displayed in the LSV curves (Fig. 2(a)), the bare carbon paper showed negligible current density, indicating the In-based catalysts were indeed the active phases for CO_2RR. Besides, the In SACs-1000 catalyst exhibited the largest current density (normalized by the geometrical surface area) in the applied potential range from −0.4 to −1.1 (V vs. V_{RHE}), implying the highest activity of the In SACs-1000 catalyst. Potentiostatic electrolysis was then conducted to evaluate the product selectivity for CO_2RR, with the gas and liquid products detected by online GC and ^{1}H NMR, respectively. Figure 2(b) shows the product distributions on different catalysts in the potential range from −0.5 to −1.0 V_{RHE} for CO_2RR. Impressively, the CO was the exclusive product over In SACs-1000 catalyst with the maximum FE_{CO} of 97% at −0.6 V_{RHE} (Fig. 2(b)). In contrast, both HCOOH and CO were detected in the case of In SACs-800, with the optimal FE_{CO} and FE_{HCOOH} of 52% (−0.5 V_{RHE}) and 38% (−0.9 V_{RHE}), respectively. As for the In_2O_3 NPs, HCOOH was the major product with the peak FE_{HCOOH} of 67.8% at −0.8 V_{RHE}. These results confirmed that these In-based catalysts presented the distinct product selectivity, evidencing the prominent implication of coordination structure on the reaction path toward CO_2RR. In order to exclude the impact of physical and chemical properties of carbon induced by different carbonization degrees on the reaction path, CO_2RR performance of nitrogen doped carbon carbonized

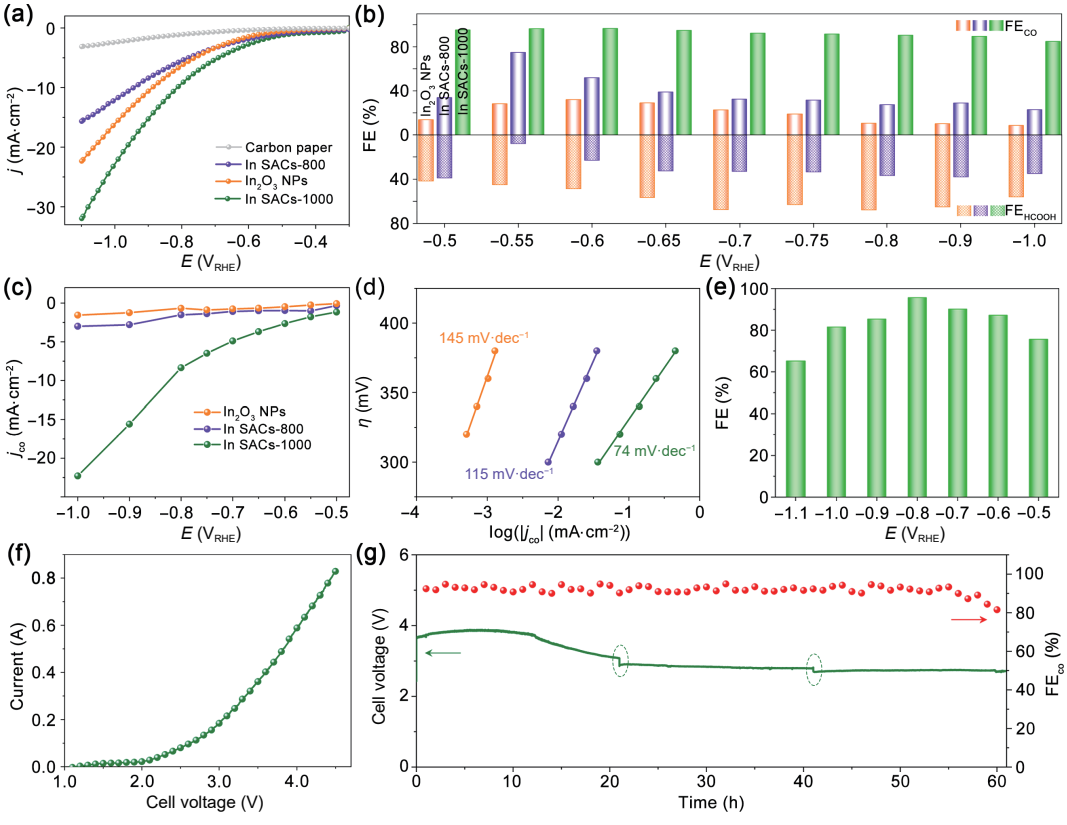

Figure 2 The CO_2RR performance of In SACs-800, In SACs-1000, and In_2O_3 catalysts. (a) LSV curves in CO_2-saturated 0.5 M $KHCO_3$ solution, scanning rate: 10 mV·s^{-1}. (b) Product selectivity under different applied potential. (c) Potential-dependent CO partial current density. (d) Tafel plots for CO formation. (e) FE_{CO} of In SACs-1000 in the flow cell (1 M KOH as electrolyte). (f) LSV curves in an anion membrane electrode assembly. (g) Durability test of the In SACs-1000 under a cell current of 0.4 A for more than 60 h continuous operation (cell voltage was presented without *iR* compensation).

under 800 and 1,000 ℃ in the absence of indium precursor was also evaluated. As presented in Fig. S12 in the ESM, similar product distribution was observed on the two nitrogen doped carbon samples, indicating that carbonization degree may not possess significant impact on the CO_2RR performance.

Since the In SACs-1000 catalyst showed gratifying FE_{CO} (more than 90%) in a wide potential range from −0.5 to −1.0 V_{RHE}, which was parallel to the state-of-the-art catalyst reported for CO production, we further analyzed the catalytic activity of these In-based catalyst for CO formation. The CO partial current density was first derived to evaluate the reaction kinetics toward CO_2 to CO conversion on these catalysts. As shown in Fig. 2(c), the In SACs-1000 catalyst exhibited a maximum CO partial current density of 22.3 mA·cm^{-2} at −1.0 V_{RHE}, which was 7.4-fold and 14.3-fold enhancements relative to In SACs-800 and In_2O_3 NPs, respectively. To figure out the origin of the great enhancements in partial current density, electrochemical C_{dl} which was typically regarded as a reference to evaluate the ECSAs was compared for the catalysts. Consistent with the similar morphology, C_{dl} of the In SACs-800 (8.1 mF·cm^{-2}) was comparable to that of In SACs-1000 (10.1 mF·cm^{-2}) (Fig. S13 in the ESM), suggesting the In SACs-1000 catalyst possessed the higher intrinsic activity toward CO production. The Tafel plots were also drawn to investigate the reaction kinetics on the CO_2RR (Fig. 2(d)). The smallest value of Tafel slope (74 mV·dec^{-1}) for the In SACs-1000 further confirmed the highest intrinsic activity for CO_2RR to CO. Moreover, the different Tafel slops also inferred distinct reaction mechanisms, where first electron transfer step for $*CO_2^-$ formation is the rate determining step (RDS) for In SACs-800 and In_2O_3 NPs while protonation of $*CO_2^-$ is the RDS for In SACs-1000 [8, 49]. Nyquist plots under the open circuit potential were also performed to gain further insight into CO_2RR kinetics. As shown in Fig. S14 in the ESM, the In SACs-1000 owned smaller interfacial charge-transfer resistance, which is favorable for the activation of adsorbed CO_2 in the first reaction step thereby leading to an accelerated Faradaic process [12]. Besides, the long-term durability test of In SACs-1000 catalyst exhibited inappreciable decays in FE_{CO} and current density after electrolysis for ~ 14 h at −0.8 V_{RHE} (Fig. S15 in the ESM), suggesting the excellent durability of the In SACs-1000 (Fig. S16 in the ESM).

Motivated by the superior catalytic performance of In SACs-1000 toward CO_2RR, efforts were further devoted to improving the current density to industrial relevant level by capitalizing on gas-fed flow cell equipped with gas diffusion electrode. It was found that the current density was significantly increased without compromising CO selectivity in the flow cell (Fig. 2(e) and Fig. S17 in the ESM). Remarkably, the CO partial current density was as high as 276 mA·cm^{-2} at −1.0 V_{RHE} (Fig. S17 in the ESM), evidencing the superiority of flow cell configuration in resolving the mass transfer restriction in typical H-type cell [50]. Besides, the FE_{CO} could reach as high as 95.6% at −0.8 V_{RHE}, placing In SACs-1000 among the best catalysts toward CO_2 to CO conversion (Table S4 in the ESM). An impressive stability of the In SACs in the flow cell was also presented in Fig. S17(d) in the ESM, the FE_{CO} fluctuated regularly with an average current density of 130 mA·cm^{-2} over 18 h continuous operating. About 20 mA·cm^{-2} attenuation of current density was observed when operating for 10 h, which could be explained by the inevitable gas diffusion electrode (GDE) flooding, catalyst deactivation as well as membrane degradation [51]. To further demonstrate its application possibility, catalytic performance of the In SACs-1000 catalyst was evaluated in a 2 cm × 2 cm membrane electrode assembly (MEA) where the anion exchange membrane was sandwiched between the two electrodes, humidified CO_2 was applied as feeding gas with 0.5 M $KHCO_3$ as anolyte [51, 52]. Owing to the minimal charge transfer resistance as well as the catholyte-free environment, industrial relevant cell current (> 100 mA·cm^{-2}) was achieved (Fig. 2(f)) and the MEA shown satisfactory durability with FE_{CO} > 90% during 60 h continuous operation at cell current of 0.4 A (Fig. 2(g)). The cell voltage was gradually decreased in the first 20 h due to the activation of the electrode catalyst and remained stable in the following 40 h, fluctuation highlighted by dash cycle in Fig. 2(g) was attributed to the electrolyte replacement. All these electrocatalytic analyses demonstrated the great potential of In SACs-1000 as a remarkable catalyst for CO_2RR to CO. More importantly, the distinct product selectivity on different In SACs implied the great impacts of coordination structure on the reaction path toward CO_2RR, which is rarely mentioned in previous works where the coordination structure typically determined the catalytic activity.

In that case, one important question is how coordination structure regulated the product selectivity. We thus employed the DFT calculations to shed light on the distinct reaction pathway over the In SACs for CO_2RR. Because the local coordination structure cannot be precisely identified by the experimental techniques, all the possible configurations of In-N_xC_{4-x} ($1 \le x \le 4$) were screened (Fig. 3(a)). Specifically, ten In-N_xC_{4-x} moieties featuring with different coordination structures in the first coordination sphere (including five pyridinic In-N_xC_{4-x} structures (denoted as pd-In-N_xC_{4-x}, Fig. S18 in the ESM) and five pyrrolic In-N_xC_{4-x} structures (denoted as pr-In-N_xC_{4-x}, Fig. S19 in the ESM) were modelled. The energy diagrams for HCOOH and CO reaction pathways on these moieties were then calculated, as shown in Fig. S20 and Table S5 in the ESM. Deriving from these calculation results, limiting potentials (U_L) for the production of CO (U_L(CO)) and HCOOH (U_L(HCOOH)) and difference between U_L(HCOOH) and U_L(CO) (U_L(HCOOH) – U_L(CO)) over different active centers were further summarized in Figs. 3(b) and 3(c), which intuitively shows the thermodynamically favorable product on each active site. Specifically, when considering the In atom as the active site, the majority of In sites favored the HCOOH formation, with pr-In-N_4-(In) sites presenting the highest activity. For CO formation, only two configurations, namely the pd-In-N_3C-(In) and pd-In-N_2C_2-trans-(In), may favor the reaction pathway from the perspective of thermodynamics. However, the reaction kinetics would be retarded given the high energy barriers (0.86 eV for pd-In-N_3C-(In) and 0.80 eV for pd-In-N_2C_2-trans-(In)) for the RDS (dehydration of *COOH to form *CO) on these active sites (Fig. S20 in the ESM). The above results suggested that the In sites may prefer the HCOOH pathway but not likely for CO pathway. Considering the contradiction between experimental data and DFT calculation result, we thus deduced the presence of active sites rather than In centers for CO formation.

Inspired by previous work where the carbon sites around the metal center in the Fe-N_4 catalyst may also function as the ORR active sites, we then shifted our attention to carbon atoms around the In center [53]. Given that the dominant nitrogen species in our In SACs is pyrrolic nitrogen, CO_2RR performance of indium-adjacent carbon atoms in pr-In-N_xC_{4-x} (denoted as pr-In-N_xC_{4-x}(C), $1 \le x \le 3$) was therefore probed by DFT simulation. Intriguingly, HCOOH formation over pr-In-N_xC_{4-x}(C) was dramatically retarded while the CO pathway was energetically favored. The pr-In-NC_3-(C2) sites exhibited the optimal CO production activity with U_L(CO) of −0.39 V, which is 0.13 V higher than corresponding U_L(HCOOH), confirming the excellent CO selectivity. Of note, the HCOOH pathway over the pr-In-N_xC_{4-x}-(In) sites was gradually blocked upon increasing carbon occupation in the first coordination sphere, which could be explained by the increased electron density on indium sites

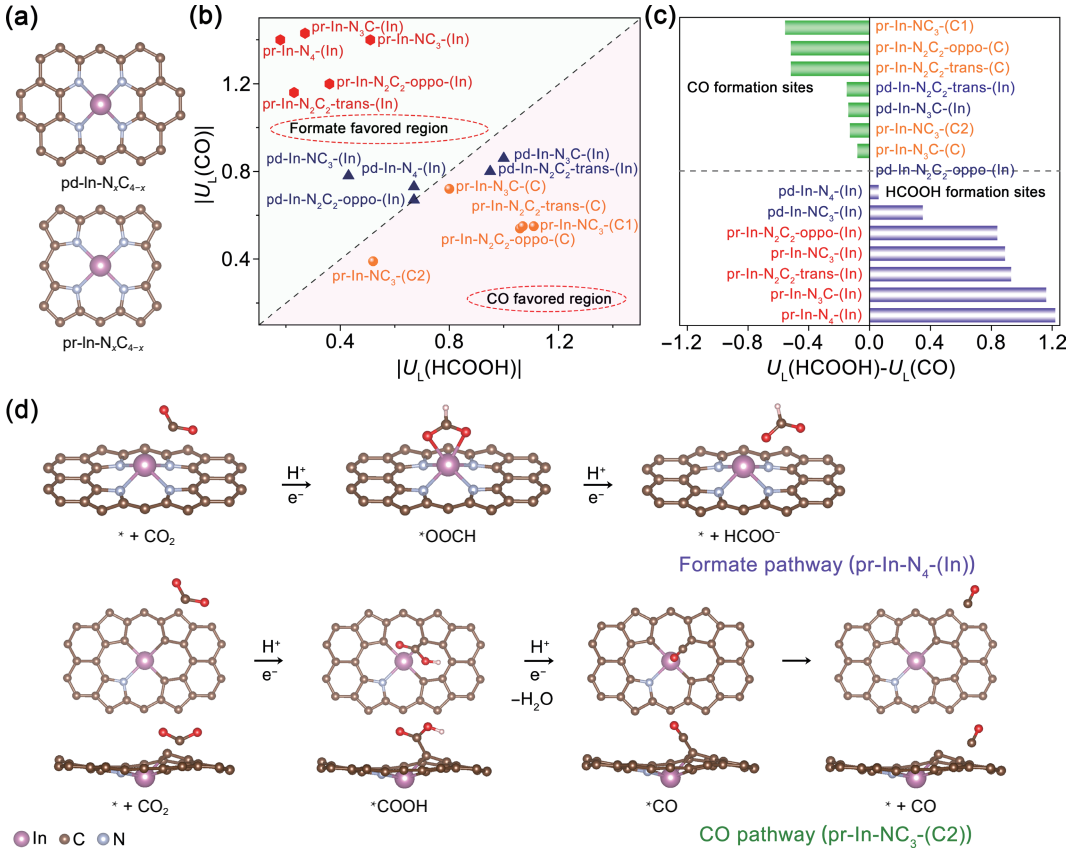

Figure 3 DFT simulation of CO_2RR activity on different sites in In SACs. (a) The computed In SACs moieties coordinated with pyridinic nitrogen (top, denoted as pd-In-N_xC_{4-x}) and pyrrolic nitrogen (bottom, pr-In-N_xC_{4-x}). (b) The limiting potentials for CO pathway (U_L(CO)) plotted against that for the HCOOH pathway (U_L(HCOOH)) on different In SACs structures shown in Figs. S18 and S19 in the ESM. (c) Difference in limiting potentials for the formation of CO and HCOOH on different In SACs moieties. (d) Proposed reaction pathways for CO_2RR on pr-In-N_4-(In) and pr-In-NC_3-(C2).

when directly coordinated with carbon with relative low electronegativity (confirmed by density of states of the indium center as shown in Fig. S21 in the ESM) [24]. We therefore propose that the active site for CO_2RR was shifted from the In center to indium-adjacent carbon atoms upon increasing carbon occupation in the first coordination sphere of In SACs, thereby shifting product selectivity from HCOOH to CO (Fig. 3(d)). Hereby, the experimental observation that In SACs-1000 catalyst with relative lower indium loading exhibited better performance toward CO production in CO_2RR was rationalized by the excellent activity of indium-adjacent carbon sites for CO generation.

Subsequently, to confirm that indium-adjacent carbon atoms are active sites for CO production in the In SACs-1000 catalyst, SCN^- which could strongly bind to the metal center thereby blocking intermediate adsorption was adopted as an indicator [45, 54–56]. Following the addition of SCN^- in CO_2 saturated 0.5 M $KHCO_3$, the current density as well as FE_{CO} of In SACs-1000 remained unchanged (Figs. 4(a)–4(c)), underlining the nonmetal-related active site. In_2O_3 NPs was employed as the reference, the significantly depressed current density as well as elevated FE_{H2} owing to the blocking of indium sites with SCN^- confirmed the strong affinity of indium toward SCN^-. Therefore, it was concluded that the indium center is not the active sites for CO_2 to CO conversion, and the excellent CO_2RR performance observed on the In SACs-1000 originated from the indium-adjacent carbon atoms (Fig. 4(d)).

4 Conclusions

In summary, we have identified a unique selectivity shift in In SACs enabled by active sites shift from the indium center to indium-adjacent carbon atoms. Specifically, the CO_2RR selectivity in In SACs was changed from HCOOH to CO upon elevating annealing temperature in the SACs fabrication process. As revealed by a combination of experimental evidences and DFT calculations, the indium center in the In SACs is active for CO_2 to HCOOH conversion, while indium-adjacent carbon atoms prefer the CO_2 to CO pathway. Since occupation of carbon atoms in the first coordination sphere would be increased by evaluating the annealing temperature, the excellent CO selectivity obtained in In SACs-1000 was rationalized by the active sites shift from the indium center to the indium-adjacent carbon atoms. This unique understanding on active sites shift in In SACs offered us new implications to revisit the origin of excellent catalytic performance of SACs, where the attention may be paid to the surrounding atoms rather than only the metal center. Beyond a remarkable catalyst for CO production, we anticipate the present work could inject new vitality not only to CO_2RR research but also the extensive electrocatalytic field.

Acknowledgements

This work was supported by the National Natural Science Foundation of China (Nos. 21905089, 2021RC3065, and 2021RC2053), the National Key Research and Development Program of China (No. 2021YFA1502000), the Science and Technology Innovation Program of Hunan Province (Nos. 2021RC3065 and 2021RC2053), Hunan Provincial Natural Science Foundation of China (No. 2020JJ2001), Shenzhen Science and Technology Program (No. JCYJ20210324120800002), and the Hefei National Laboratory for Physical Sciences at the Microscale (No. KF2020108). The calculations were performed on the supercomputing center of the University of Science and Technology of China (USTC-SCC) and Guangzhou-SCC.

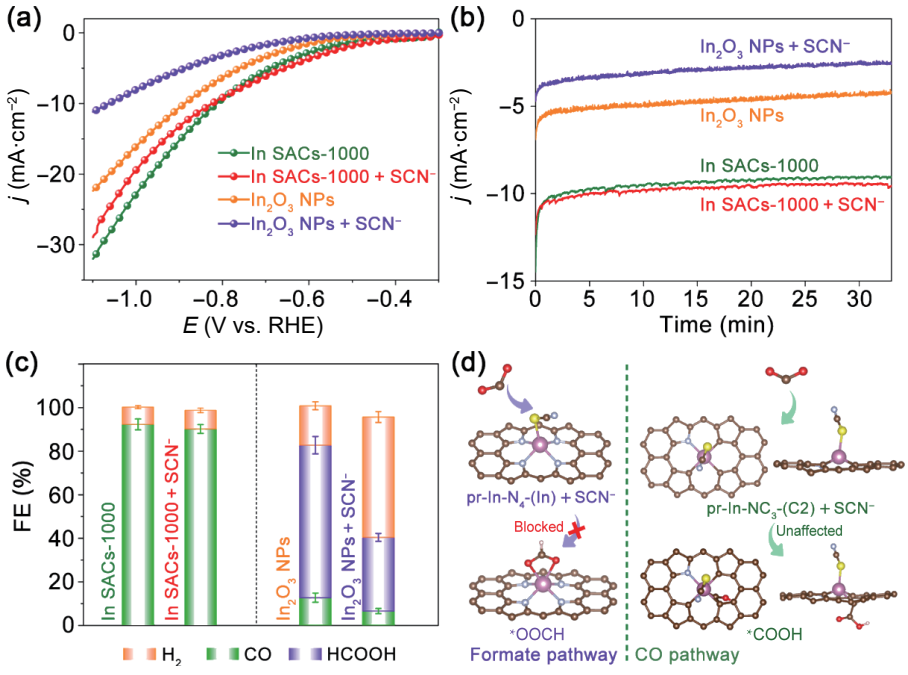

Figure 4 Active sites poisoning experiments. (a) LSV curves of In SACs-1000 and In_2O_3 NPs before and after the addition of 0.02 M KSCN in CO_2-saturated 0.5 M $KHCO_3$. (b) Current density and (c) product selectivity of In SACs-1000 and In_2O_3 at −0.8 V_{RHE} with or without 0.02 M KSCN. (d) The CO_2RR reaction pathway for pr-In-N_4-(In) and pr-In-NC_3-(C2) in the presence of KSCN.

Electronic Supplementary Material: Supplementary material (TEM imaging, XRD and XPS characterization, and calculations details) is available in the online version of this article at https://doi.org/10.1007/s12274-022-4177-x.

References

[1] Franco, F.; Rettenmaier, C.; Jeon, H. S.; Roldan Cuenya, B. Transition metal-based catalysts for the electrochemical CO_2 reduction: From atoms and molecules to nanostructured materials. *Chem. Soc. Rev.* **2020**, *49*, 6884–6946.

[2] De Luna, P.; Hahn, C.; Higgins, D.; Jaffer, S. A.; Jaramillo, T. F.; Sargent, E. H. What would it take for renewably powered electrosynthesis to displace petrochemical processes? *Science* **2019**, *364*, eaav3506.

[3] Shih, C. F.; Zhang, T.; Li, J. H.; Bai, C. L. Powering the Future with Liquid Sunshine. *Joule* **2018**, *2*, 1925–1949.

[4] Yang, H. P.; Wu, Y.; Lin, Q.; Fan, L. D.; Chai, X. Y.; Zhang, Q. L.; Liu, J. H.; He, C. X.; Lin, Z. Q. Composition tailoring via N and S co-doping and structure tuning by constructing hierarchical pores: Metal-free catalysts for high-performance electrochemical reduction of CO_2. *Angew. Chem., Int. Ed.* **2018**, *57*, 15476–15480.

[5] Zhang, M.; Xuan, X. X.; Wang, W. L.; Ma, C. Y.; Lin, Z. Q. Anode photovoltage compensation-enabled synergistic CO_2 photoelectrocatalytic reduction on a flower-like graphene-decorated Cu foam cathode. *Adv. Funct. Mater.* **2020**, *30*, 2005983.

[6] Nitopi, S.; Bertheussen, E.; Scott, S. B.; Liu, X. Y.; Engstfeld, A. K.; Horch, S.; Seger, B.; Stephens, I. E. L.; Chan, K.; Hahn, C. et al. Progress and perspectives of electrochemical CO_2 reduction on copper in aqueous electrolyte. *Chem. Rev.* **2019**, *119*, 7610–7672.

[7] Masel, R. I.; Liu, Z. C.; Yang, H. Z.; Kaczur, J. J.; Carrillo, D.; Ren, S. X.; Salvatore, D.; Berlinguette, C. P. An industrial perspective on catalysts for low-temperature CO_2 electrolysis. *Nat. Nanotechnol.* **2021**, *16*, 118–128.

[8] Zhang, Y.; Guo, S. X.; Zhang, X. L.; Bond, A. M.; Zhang, J. Mechanistic understanding of the electrocatalytic CO_2 reduction reaction-New developments based on advanced instrumental techniques. *Nano Today* **2020**, *31*, 100835.

[9] Yu, D.; Gao, L.; Sun, T. L.; Guo, J. C.; Yuan, Y. L.; Zhang, J. W.; Li, M. F.; Li, X. X.; Liu, M. C.; Ma, C. et al. Strain-stabilized metastable face-centered tetragonal gold overlayer for efficient CO_2 electroreduction. *Nano Lett.* **2021**, *21*, 1003–1010.

[10] Yoshio, H.; Katsuhei, K.; Akira, M.; Shin, S. Production of methane and ethylene in electrochemical reduction of carbon dioxide at copper electrode in aqueous hydrogencarbonate solution. *Chem. Lett.* **1986**, *15*, 897–898.

[11] Yoshio, H.; Katsuhei, K.; Shin, S. Production of CO and CH_4 in electrochemical reduction of CO_2 at metal electrodes in aqueous hydrogencarbonate solution. *Chem. Lett.* **1985**, *14*, 1695–1698.

[12] Asadi, M.; Kim, K.; Liu, C.; Addepalli, A. V.; Abbasi, P.; Yasaei, P.; Phillips, P.; Behranginia, A.; Cerrato, J. M.; Haasch, R. et al. Nanostructured transition metal dichalcogenide electrocatalysts for CO_2 reduction in ionic liquid. *Science* **2016**, *353*, 467–470.

[13] Chen, J. Y.; Wang, T. T.; Li, Z. J.; Yang, B.; Zhang, Q. H.; Lei, L. C.; Feng, P. Y.; Hou, Y. Recent progress and perspective of electrochemical CO_2 reduction towards C_2-C_5 products over non-precious metal heterogeneous electrocatalysts. *Nano Res.* **2021**, *14*, 3188–3207.

[14] Gao, D. F.; Zhou, H.; Wang, J.; Miao, S.; Yang, F.; Wang, G. X.; Wang, J. G.; Bao, X. H. Size-dependent electrocatalytic reduction of CO_2 over Pd nanoparticles. *J. Am. Chem. Soc.* **2015**, *137*, 4288–4291.

[15] Zhu, W. L.; Zhang, Y. J.; Zhang, H. Y.; Lv, H. F.; Li, Q.; Michalsky, R.; Peterson, A. A.; Sun, S. H. Active and selective conversion of CO_2 to CO on ultrathin Au nanowires. *J. Am. Chem. Soc.* **2014**, *136*, 16132–16135.

[16] Back, S.; Lim, J.; Kim, N. Y.; Kim, Y. H.; Jung, Y. Single-atom catalysts for CO_2 electroreduction with significant activity and selectivity improvements. *Chem. Sci.* **2017**, *8*, 1090–1096.

[17] Varela, A. S.; Ju, W.; Bagger, A.; Franco, P.; Rossmeisl, J.; Strasser, P. Electrochemical reduction of CO_2 on metal-nitrogen-doped carbon catalysts. *ACS Catal.* **2019**, *9*, 7270–7284.

[18] Zhang, Z.; Ma, C.; Tu, Y. C.; Si, R.; Wei, J.; Zhang, S. H.; Wang, Z.; Li, J. F.; Wang, Y.; Deng, D. H. Multiscale carbon foam confining single iron atoms for efficient electrocatalytic CO_2 reduction to CO. *Nano Res.* **2019**, *12*, 2313–2317.

[19] Zhang, J. C.; Cai, W. Z.; Hu, F. X.; Yang, H. B.; Liu, B. Recent advances in single atom catalysts for the electrochemical carbon dioxide reduction reaction. *Chem. Sci.* **2021**, *12*, 6800–6819.

[20] Su, X.; Yang, X. F.; Huang, Y. Q.; Liu, B.; Zhang, T. Single-atom catalysis toward efficient CO_2 conversion to CO and formate products. *Acc. Chem. Res.* **2019**, *52*, 656–664.

[21] Chen, S. H.; Li, W. H.; Jiang, W. J.; Yang, J. R.; Zhu, J. X.; Wang, L. Q.; Ou, H. H.; Zhuang, Z. C.; Chen, M. Z.; Sun, X. H. et al. MOF encapsulating N-heterocyclic carbene-ligated copper single-atom site catalyst towards efficient methane electrosynthesis. *Angew. Chem., Int. Ed.* **2022**, *61*, e202114450.

[22] Sun, X. H.; Tuo, Y. X.; Ye, C. L.; Chen, C.; Lu, Q.; Li, G. N.; Jiang, P.; Chen, S. H.; Zhu, P.; Ma, M. et al. Phosphorus induced electron localization of single iron sites for boosted CO_2 electroreduction reaction. *Angew. Chem., Int. Ed.* **2021**, *60*, 23614–23618.

[23] Jiang, K.; Siahrostami, S.; Zheng, T. T.; Hu, Y. F.; Hwang, S.; Stavitski, E.; Peng, Y. D.; Dynes, J.; Gangisetty, M.; Su, D. et al. Isolated Ni single atoms in graphene nanosheets for high-performance CO_2 reduction. *Energy Environ. Sci.* **2018**, *11*, 893–903.

[24] Jiang, K.; Siahrostami, S.; Akey, A. J.; Li, Y. B.; Lu, Z. Y.; Lattimer, J.; Hu, Y. F.; Stokes, C.; Gangishetty, M.; Chen, G. X. et al. Transition-metal single atoms in a graphene shell as active centers for highly efficient artificial photosynthesis. *Chem* **2017**, *3*, 950–960.

[25] Zhang, E. H.; Wang, T.; Yu, K.; Liu, J.; Chen, W. X; Li, A.; Rong, H. P.; Lin, R.; Ji, S. F.; Zheng, X. S. et al. Bismuth single atoms resulting from transformation of metal-organic frameworks and their use as electrocatalysts for CO_2 reduction. *J. Am. Chem. Soc.* **2019**, *141*, 16569–16573.

[26] Cui, X.; Gao, L. K.; Lei, S.; Liang, S.; Zhang, J. W.; Sewell, C. D.; Xue, W. D.; Liu, Q.; Lin, Z. Q.; Yang, Y. K. Simultaneously crafting single-atomic fe sites and graphitic layer-wrapped Fe_3C nanoparticles encapsulated within mesoporous carbon tubes for oxygen reduction. *Adv. Funct. Mater.* **2021**, *31*, 2009197.

[27] Qu, Q. Y.; Ji, S. F.; Chen, Y. J.; Wang, D. S.; Li, Y. D. The atomic-level regulation of single-atom site catalysts for the electrochemical CO_2 reduction reaction. *Chem. Sci.* **2021**, *12*, 4201–4215.

[28] Li, X. Y.; Rong, H. P.; Zhang, J. T.; Wang, D. S.; Li, Y. D. Modulating the local coordination environment of single-atom catalysts for enhanced catalytic performance. *Nano Res.* **2020**, *13*, 1842–1855.

[29] Hu, M. Y.; Li, S. N.; Zheng, S. S.; Liang, X. H.; Zheng, J. X.; Pan, F. Tuning single-atom catalysts of nitrogen-coordinated transition metals for optimizing oxygen evolution and reduction reactions. *J. Phys. Chem. C* **2020**, *124*, 13168–13176.

[30] Shang, H. S.; Zhou, X. Y.; Dong, J. C.; Li, A.; Zhao, X.; Liu, Q. H.; Lin, Y.; Pei, J. J.; Li, Z.; Jiang, Z. L. et al. Engineering unsymmetrically coordinated $Cu\text{-}S_1N_3$ single atom sites with enhanced oxygen reduction activity. *Nat. Commun.* **2020**, *11*, 3049.

[31] Pan, Y.; Chen, Y. J.; Wu, K. L.; Chen, Z.; Liu, S. J.; Cao, X.; Cheong, W. C.; Meng, T.; Luo, J.; Zheng, L. R. et al. Regulating the coordination structure of single-atom $Fe\text{-}N_xC_y$ catalytic sites for benzene oxidation. *Nat. Commun.* **2019**, *10*, 4290.

[32] Zhang, J. T.; Zhang, M.; Zeng, Y.; Chen, J. S.; Qiu, L. X.; Zhou, H.; Sun, C. J.; Yu, Y.; Zhu, C. Z.; Zhu, Z. H. Single Fe atom on hierarchically porous S, N-codoped nanocarbon derived from porphyra enable boosted oxygen catalysis for rechargeable Zn-Air batteries. *Small* **2019**, *15*, 1900307.

[33] Wang, X. Q.; Chen, Z.; Zhao, X. Y.; Yao, T.; Chen, W. X.; You, R.; Zhao, C. M.; Wu, G.; Wang, J.; Huang, W. X. et al. Regulation of coordination number over single co sites: Triggering the efficient electroreduction of CO_2. *Angew. Chem., Int. Ed.* **2018**, *57*, 1944–1948.

[34] Rong, X.; Wang, H. J.; Lu, X. L.; Si, R.; Lu, T. B. Controlled synthesis of a vacancy-defect single-atom catalyst for boosting CO_2 electroreduction. *Angew. Chem., Int. Ed.* **2020**, *59*, 1961–1965.

[35] Jia, M. W.; Hong, S.; Wu, T. S.; Li, X.; Soo, Y. L.; Sun, Z. Y. Single Sb sites for efficient electrochemical CO_2 reduction. *Chem. Commun.* **2019**, *55*, 12024–12027.

[36] Jiang, Z. L.; Wang, T.; Pei, J. J.; Shang, H. S.; Zhou, D. N.; Li, H. J.; Dong, J. C.; Wang, Y.; Cao, R.; Zhuang, Z. B. et al. Discovery of main group single $Sb\text{-}N_4$ active sites for CO_2 electroreduction to formate with high efficiency. *Energy Environ. Sci.* **2020**, *13*, 2856–2863.

[37] Tang, C.; Chen, L.; Li, H. J.; Li, L. Q.; Jiao, Y.; Zheng, Y.; Xu, H. L.; Davey, K.; Qiao, S. Z. Tailoring acidic oxygen reduction selectivity on single-atom catalysts via modification of first and second coordination spheres. *J. Am. Chem. Soc.* **2021**, *143*, 7819–7827.

[38] Jing, H. Y.; Zhu, P.; Zheng, X. B.; Zhang, Z. D.; Wang, D. S.; Li, Y. D. Theory-oriented screening and discovery of advanced energy transformation materials in electrocatalysis. *Adv. Powder Mater.*, in press, DOI:10.1016/j.apmate.2021.10.004.

[39] Wang, Y.; Zheng, X. B.; Wang, D. S. Design concept for electrocatalysts. *Nano Res.* **2022**, *15*, 1730–1752.

[40] Jing, H. Y.; Zhao, Z. Y.; Zhang, J. W.; Zhu, C.; Liu, W.; Li, N. N.; Hao, C.; Shi, Y. T.; Wang, D. S. Atomic evolution of metal-organic frameworks into $CO\text{-}N_3$ coupling vacancies by cooperative cascade protection strategy for promoting triiodide reduction. *J. Phys. Chem. C* **2021**, *125*, 6147–6156.

[41] Jing, H. Y.; Liu, W.; Zhao, Z. Y.; Zhang, J. W.; Zhu, C.; Shi, Y. T.; Wang, D. S.; Li, Y. D. Electronics and coordination engineering of atomic cobalt trapped by oxygen-driven defects for efficient cathode in solar cells. *Nano Energy* **2021**, *89*, 106365.

[42] Lu, P. L.; Tan, X.; Zhao, H. T.; Xiang, Q.; Liu, K. L.; Zhao, X. X.; Yin, X. M.; Li, X. Z.; Hai, X.; Xi, S. B. et al. Atomically dispersed indium sites for selective CO_2 electroreduction to formic acid. *ACS Nano* **2021**, *15*, 5671–5678.

[43] Wang, H.; Jia, J.; Song, P. F.; Wang, Q.; Li, D. B.; Min, S. X.; Qian, C. X.; Wang, L.; Li, Y. F.; Ma, C. et al. Efficient electrocatalytic reduction of CO_2 by nitrogen-doped nanoporous carbon/carbon nanotube membranes: A step towards the electrochemical CO_2 Refinery. *Angew. Chem., Int. Ed.* **2017**, *56*, 7847–7852.

[44] Yang, H. P.; Wu, Y.; Li, G. D.; Lin, Q.; Hu, Q.; Zhang, Q. L.; Liu, J. H.; He, C. X. Scalable production of efficient single-atom copper decorated carbon membranes for CO_2 electroreduction to methanol. *J. Am. Chem. Soc.* **2019**, *141*, 12717–12723.

[45] Shang, H. S.; Wang, T.; Pei, J. J.; Jiang, Z. L.; Zhou, D. N.; Wang, Y.; Li, H. J.; Dong, J. C.; Zhuang, Z. B.; Chen, W. X. et al. Design of a single-atom $indium^{\delta+}\text{-}N_4$ interface for efficient electroreduction of CO_2 to formate. *Angew. Chem., Int. Ed.* **2020**, *59*, 22465–22469.

[46] Guo, W. W.; Tan, X. X.; Bi, J. H.; Xu, L.; Yang, D. X.; Chen, C. J.; Zhu, Q. G.; Ma, J.; Tayal, A.; Ma, J. Y. et al. Atomic indium catalysts for switching CO_2 electroreduction products from formate to CO. *J. Am. Chem. Soc.* **2021**, *143*, 6877–6885.

[47] Luo, F.; Roy, A.; Silvioli, L.; Cullen, D. A.; Zitolo, A.; Sougrati, M. T.; Oguz, I. C.; Mineva, T.; Teschner, D.; Wagner, S. et al. *P*-block single-metal-site tin/nitrogen-doped carbon fuel cell cathode catalyst for oxygen reduction reaction. *Nat. Mater.* **2020**, *19*, 1215–1223.

[48] Ren, W. H.; Tan, X.; Yang, W. F.; Jia, C.; Xu, S. M.; Wang, K. X.; Smith, S. C.; Zhao, C. Isolated diatomic Ni-Fe metal-nitrogen sites for synergistic electroreduction of CO_2. *Angew. Chem., Int. Ed.* **2019**, *58*, 6972–6976.

[49] Lu, Q.; Rosen, J.; Zhou, Y.; Hutchings, G. S.; Kimmel, Y. C.; Chen, J. G.; Jiao, F. A selective and efficient electrocatalyst for carbon dioxide reduction. *Nat. Commun.* **2014**, *5*, 3242.

[50] Liu, K.; Smith, W. A.; Burdyny, T. Introductory guide to assembling and operating gas diffusion electrodes for electrochemical CO_2 reduction. *ACS Energy Lett.* **2019**, *4*, 639–643.

[51] Zheng, T. T.; Jiang, K.; Ta, N.; Hu, Y. F.; Zeng, J.; Liu, J. Y.; Wang, H. T. Large-scale and highly selective CO_2 electrocatalytic reduction on nickel single-atom catalyst. *Joule* **2019**, *3*, 265–278.

[52] Gabardo, C. M.; O'Brien, C. P.; Edwards, J. P.; McCallum, C.; Xu, Y.; Dinh, C. T.; Li, J.; Sargent, E. H.; Sinton, D. Continuous carbon

dioxide electroreduction to concentrated multi-carbon products using a membrane electrode assembly. *Joule* **2019**, *3*, 2777–2791.

[53] Yang, L.; Cheng, D. J.; Xu, H. X.; Zeng, X. F.; Wan, X.; Shui, J. L.; Xiang, Z. H.; Cao, D. P. Unveiling the high-activity origin of single-atom iron catalysts for oxygen reduction reaction. *Proc. Natl. Acad. Sci. USA* **2018**, *115*, 6626–6631.

[54] Zhang, B. X.; Zhang, J. L.; Shi, J. B.; Tan, D. X.; Liu, L. F.; Zhang, F. Y.; Lu, C.; Su, Z. Z.; Tan, X. N.; Cheng, X. Y. et al. Manganese acting as a high-performance heterogeneous electrocatalyst in carbon dioxide reduction. *Nat. Commun.* **2019**, *10*, 2980.

[55] Ni, W. P.; Liu, Z. X.; Zhang, Y.; Ma, C.; Deng, H. Q.; Zhang, S. G.; Wang, S. Y. Electroreduction of carbon dioxide driven by the intrinsic defects in the carbon plane of a single Fe-N_4 site. *Adv. Mater.* **2021**, *33*, 2003238.

[56] Liu, C.; Li, H.; Liu, F.; Chen, J. S.; Yu, Z. X.; Yuan, Z. W.; Wang, C. J.; Zheng, H. L.; Henkelman, G.; Wei, L. et al. Intrinsic activity of metal centers in metal-nitrogen-carbon single-atom catalysts for hydrogen peroxide synthesis. *J. Am. Chem. Soc.* **2020**, *142*, 21861–21871.